



Mesoscopic discrete modeling of multiaxial load-induced thermal strain of concrete at high temperature

Lei Shen ^{a,*}, Huayi Zhang ^a, Giovanni Di Luzio ^b, Hao Yin ^c, Lifu Yang ^a, Gianluca Cusatis ^c

^a Hohai University, College of Water Conservancy and Hydropower Engineering, Nanjing, 210098, China

^b Politecnico di Milano, Department of Civil and Environmental Engineering, Milan, 20121, Italy

^c Northwestern University, Department of Civil and Environmental Engineering, Evanston, IL, 60208, USA

ARTICLE INFO

Keywords:

Lattice discrete particle model
Load-induced thermal strain
High temperature
Transient thermal creep
Multiaxial loading

ABSTRACT

This work presents a mesoscopic discrete model of load-induced thermal strain (LITS) as part of the Lattice Discrete Particle Model at high temperature (LDPM-HT) that captures the experimentally observed deformations and mechanical responses of concrete heating up to 800 °C under multiaxial loads. In the proposed model, the LITS is decoupled into elastic strain increment due to thermal degradation, and thermo-mechanical strain at the mesoscale. As the most important component, the mesoscopic thermo-mechanical strain is decomposed into a normal and two shear components. The normal component in compression of the thermo-mechanical deformation at the mesoscale controls the macroscopic LITS in the load direction, while the mesoscopic thermo-mechanical strain components in normal tension and shear directions dominate the macroscopic LITS in the unloaded directions. The correctness and accuracy of the improved LDPM-HT are demonstrated by simulating two experimental investigations, namely a heating test up to 800 °C with uniaxial load and a heating test up to 250 °C with multiaxial loads.

1. Introduction

The behavior of concrete changes significantly at high temperatures, e.g. strength and stiffness decrease generally with temperature, as well as the deformation characteristics modifies significantly at high temperatures [1,2]. Experimental results revealed that strength, stiffness and creep depend on the combination of the load and temperature histories. In particular, the load-induced thermal strain (LITS) is the additional strain that develops when stressed concrete is heated. Its existence was experimentally discovered by Hansen and Eriksson [3] in the mid 60's of the last century. LITS is significantly important in the behavior of concrete structures subject to high temperatures heating-cooling cycles under sustained compressive loads. On one hand, its effects may be beneficial during the first heating because LITS mitigates the additional compressive stresses appearing in structural elements that present some restraint to thermal expansion, as well as, at the material level, LITS in the cement paste prevents the localization of high compressive stresses [4–6]. On the other hand, since LITS is mainly irrecoverable with the temperature, this can cause important damage during the cooling phase both at material level and at structural level for restrained structures in which high tensile stresses would develop for the heating-cooling cycle [7].

When concrete is heated in the absence of any mechanical load, it exhibits a volumetric thermal strain usually referred to the Free Thermal Strain (FTS). Such strain is overall expansive as an interactional result of different phenomena of various material components, such as the shrinkage of cement paste and the expansion of aggregates [8,9]. Considering the deformation due to a mechanical load, it depends strongly when the load is applied. If concrete is heated under loading, it exhibits much larger strains than the case in which it is first heated and then loaded. This means that the combined effects of stress and elevated temperature cannot be expressed simply as the sum of the effects of variable temperature under zero stress and stress under constant temperature. This phenomenon, which is termed *transitional thermal creep*, is analogous to the well-known Pickett effect in drying creep [8,10–12]. The transitional thermal creep can be seen as a stress-induced thermal expansion and, in this case, it is often interpreted as the load-induced thermal strain (LITS). For sealed concrete under temperatures below 100 °C, Illston and Sanders [13] were the first to report about the nature and properties of this phenomenon naming it *transitional thermal creep*. Transitional thermal creep, which represents a transient increase of creep after a temperature change (both heating and cooling), develops irrecoverably during the first-time heating of sealed concrete under load for a few days. The physical source of

* Corresponding author.

E-mail address: shenl@hhu.edu.cn (L. Shen).

<https://doi.org/10.1016/j.ijmecsci.2022.107613>

Received 24 February 2022; Received in revised form 13 July 2022; Accepted 3 August 2022

Available online 8 August 2022

0020-7403/© 2022 Elsevier Ltd. All rights reserved.

Nomenclature

α^s	Shear-normal coupling parameter
α^{th}	Linear thermal expansion coefficient
β^{th}	Thermal expansion coefficient in compression
γ^{th}	Thermal expansion coefficient in tension
ω	Degree of interaction between shear and normal loading
σ_0	Mesoscopic tension-shear strength limit
σ_{bc}	Mesoscopic compression stress boundary
σ_{bt}	Mesoscopic tension stress boundary
\mathbf{e}	Total strain tensor with components e_N e_M e_L
\mathbf{e}^{fth}	Free thermal strain tensor, FTS
\mathbf{e}^{sh}	Shrinkage strain tensor
\mathbf{e}^s	Mechanical strain tensor
\mathbf{e}^{thm}	Thermo-mechanical strain tensor with components e_N^{thm} e_M^{thm} e_L^{thm}
\mathbf{e}^v	Time-dependent creep strain tensor
\mathbf{t}^s	Stress tensor with components t_N^s t_M^s t_L^s
Θ	Normalized Temperature level
θ	Temperature level
Λ	Thermal degradation function
φ_p	Mesoscopic compression-shear plastic potential
E_N, E_T	Effective normal and shear elastic modulus
H_t, H_c	Mesoscopic tension softening and compression hardening modulus
n_d	Thermal degradation shape coefficient
T	Temperature
T_s, T_m	Temperature at which concrete starts to degrade and melt
e^s	Effective mechanical strain
e_N^s, e_T^s	Effective normal and shear mechanical strain
e_V^s, e_D^s	Volumetric and deviatoric strain caused by stress
t_N^+, t_N^-	Positive and negative part of normal stress
t^s	Effective stress
t_N^s, t_T^s	Effective normal and shear stress

this effect involves two different mechanisms [14]: (1) an apparent macroscopic mechanism, due to thermally induced micro-cracking; (2) a nanoscale mechanism due to a change in the level of microprestress caused by a change of chemical potential of nanopore water with a temperature change [15,16]. Also in unsealed concrete during first heating to temperatures considerably above 100 °C transitional thermal creep occurs irreversibly. Under unsealed condition moisture drying occurs with the concurrent development of drying creep. Therefore, in unsealed concrete the term *transient creep* is more appropriate to denote the combined effects of transitional thermal creep and drying creep. It can be assumed that the transient creep response of concrete is quasi-instantaneous and, for practical applications, can be considered as time-independent and a function of the change in temperature and moisture transport [5,17,18]. In this aspect, the transient creep seems to differ from transitional thermal creep which develops more slowly at temperatures below 100 °C.

LITS comprises transient creep, basic creep and changes in the elastic strain due to the thermal degradation of the elastic modulus of the concrete components [4,18,19]. Although there is no certainty of the mechanisms behind those phenomena, the transient creep represents the biggest component of LITS and it is usually assumed that it is caused

mainly by drying of the cement matrix between 100 °C and 200 °C (drying creep), while for higher temperatures the physical disintegration and the changes of the chemical structure of the hydrates is primarily source of it. The extensive experimental campaigns were conducted by Anderberg and Thelandersson [20], Anderberg and Thelandersson [21], Schneider [4,22], Petkovski and Crouch [23], Mindeguia et al. [24], Khoury et al. [5]. Based on the experimental observations, LITS is typically empirically modeled as a quasi-instantaneous stress-induced thermal strain which develops on the heating temperature and compressive stress level [20–22,24–26].

In the literature, most of the available experimental investigations [5,21,23] and numerical studies [17,27,28] focus on the development of LITS for uniaxial compressive stress states at macro-scale, providing a good basis for assessing the behavior of concrete framed structures. However, little attention has been paid to understand the LITS of concrete under multiaxial compressive loads. With this in mind, this work presents a novel mesoscopic constitutive law to improve the Lattice Discrete Particle Model at High Temperature (LDPM-HT) [9,29] to predict the LITS in concrete under general multiaxial loading. At the macro-scale, LITS in the compression direction increases with the raising stress level and temperature. However, in uniaxial test also an expansive LITS in the load-free direction (perpendicular to the compression) is typically observed leading to the definition of LITS Poisson's ratio, ν_{LITS} , analogous to the Elastic Poisson's ratio [19,26,27,30]. Unfortunately, the evolution of LITS in the unloaded direction with the temperature is not proportional to LITS in the loaded direction, i.e. ν_{LITS} is not constant [23,26,31,32]. To reproduce this behavior some multiaxial generalization of the uniaxial model were developed in the past [21,26,33–38]. The macroscopic mechanics of concrete subjected to temperature loading is quite complex and macroscopic constitutive laws, which are based on existing experimental results, cannot be relied upon to predict the structural response outside the range of these experiments. This calls for meso-scale multi-physic approach. However, the meso-scale models in the literature [39–41] are limited and they typically focused on to the case of uniaxial compression without paying close attention to the multiaxial LITS.

Despite the considerable research efforts over the last years, a comprehensive numerical model able to simulate the deformation multiaxial behavior of concrete with and with loading under high temperature is still lacking. This paper aims to fill this gap by providing in the present work an update of the mesoscale model LDPM-HT [9,29,42] to simulate the thermal deformation of concrete subjected to multiaxial loads, in which the LITS is described as the combined result of the normal compression, normal tension and shear thermal strains at the meso-scale. Two experimental investigation from the literature are adopted to calibrate and validate this model, namely the concrete under uniaxial compression heated up to 800 °C Anderberg and Thelandersson [21] and the concrete under multiaxial compression heated up to 250 °C [23].

2. Modified LDPM-HT

The Lattice Discrete Particle Model for High Temperature (LDPM-HT) is a discrete mesoscale model that was formulated in the framework of LDPM [43–47] and it was successfully employed to simulate numerically the behavior of concrete at high temperature in terms of spalling behavior [9] and moisture migration during heating [29]. In this research work, the LDPM-HT is further improved to capturing the LITS and mechanical responses of concrete under multiaxial loads. In this section, the LDPM-HT formulation is presented emphasizing the new features that are introduced in the model.

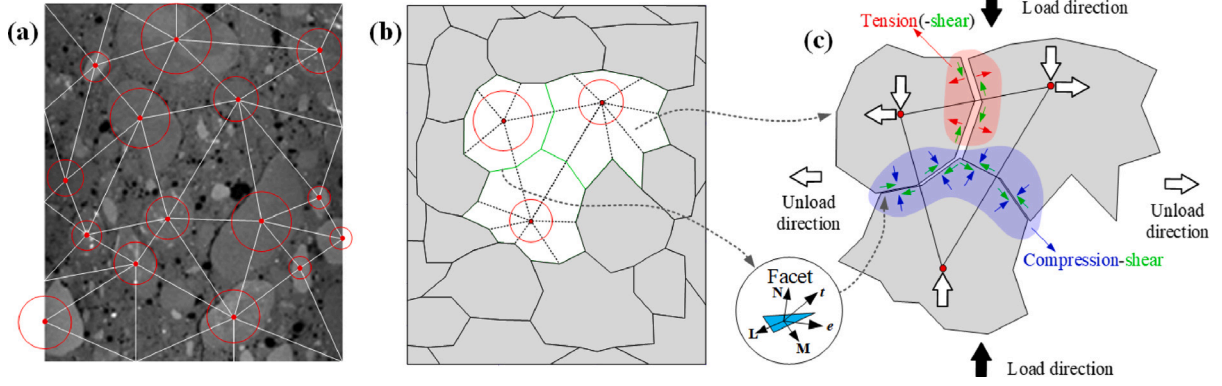


Fig. 1. Illustrations of LDPM discretization. (a) Distribution of aggregates; (b) Cell system; (c) Strain incompatibility.

2.1. Meso-scale discretization

LDPM simulates the concrete mesostructure by taking into account the interaction of coarse aggregate pieces, which are approximated by spheres of different sizes and randomly placed inside the concrete volume. The random placement of aggregates follows the actual particle size distribution curve fitted using a Fuller sieve curve as shown in Fig. 1(a). A Delaunay tetrahedralization generates tetrahedra by connecting the centers of the spherical particles. The tetrahedra edges produces a lattice system which characterizes the interaction between adjacent particles. In Fig. 1(b), a domain tessellation is performed to define potential failure locations, i.e. 12 triangular area called “facets” with unit normal vector \mathbf{n} and shear vectors \mathbf{m} and \mathbf{l} in each tetrahedron. By connecting the facets surrounding each aggregate center, a system of polyhedral cells is obtained.

2.2. Strain decomposition

If \mathbf{x}_i and \mathbf{x}_j are the positions of nodes (aggregate centers) i and j , adjacent to a generic facet, the facet strains are defined as:

$$\mathbf{e} = [e_N \ e_M \ e_L]^T = \left[\frac{\mathbf{n}^T \llbracket \mathbf{u} \rrbracket}{l} \ \frac{\mathbf{m}^T \llbracket \mathbf{u} \rrbracket}{l} \ \frac{\mathbf{l}^T \llbracket \mathbf{u} \rrbracket}{l} \right]^T \quad (1)$$

where e_N is the normal strain component, e_M and e_L are the tangential strain components, $\llbracket \mathbf{u} \rrbracket = \mathbf{u}_j - \mathbf{u}_i$ is the displacement jump at the centroid of the facet, $l = \|\mathbf{x}_j - \mathbf{x}_i\|_2$ is the distance between the two nodes, $\mathbf{n} = (\mathbf{x}_j - \mathbf{x}_i)/l$, and \mathbf{m} , \mathbf{l} are two unit vectors mutually orthogonal and orthogonally to \mathbf{n} . The displacements \mathbf{u}_i and \mathbf{u}_j are calculated as a function of translational and rotational degrees of freedom of the particles through rigid body kinematics.

Assuming the superposition theory [11,48], the total strain rate, $\dot{\mathbf{e}}$, observed under first time heating at high temperature can be considered to be the sum of the various strain components:

$$\dot{\mathbf{e}} = \dot{\mathbf{e}}^s + \dot{\mathbf{e}}^{fth} + \dot{\mathbf{e}}^{sh} + \dot{\mathbf{e}}^v + \dot{\mathbf{e}}^{thm} \quad (2)$$

where $\dot{\mathbf{e}}^s$ is the mechanical strain rate, $\dot{\mathbf{e}}^{fth}$ is the free thermal strain rate, $\dot{\mathbf{e}}^v$ is the creep strain rate, $\dot{\mathbf{e}}^{sh}$ is the shrinkage strain, and $\dot{\mathbf{e}}^{thm}$ is the thermo-mechanical strain rate. The strain rate $\dot{\mathbf{e}}^s$ depends on the tractions \mathbf{t}^s acting on the solid skeleton through a vectorial constitute equation $\mathbf{t}^s = \mathbf{f}(\mathbf{e}^s)$; see in Section 2.3. The sum of the two terms, $\dot{\mathbf{e}}^v$ and $\dot{\mathbf{e}}^{thm}$, comprises the LITS rate, in which the latter is observed only during first heating and not during subsequent cooling or heating cycles [5]. The shrinkage strain rate component, $\dot{\mathbf{e}}^{sh}$, which is independent of loading, is not explicitly considered in this formulation since all experimental high temperature data are reported from unsealed test conditions and the shrinkage contribution is included in the thermal strain.

The strain rate, $\dot{\mathbf{e}}^{fth}$, on facets that describes the free thermal deformation without mechanical loads is expressed as:

$$\dot{\mathbf{e}}^{fth} = [\alpha^{th}(T) \ 0 \ 0]^T \dot{T} \quad (3)$$

in which, T is the temperature in $^\circ\text{C}$, \dot{T} is the temperature rate and $\alpha^{th}(T)$ is the linear thermal expansion coefficient. $\alpha^{th}(T)$ is actually an overall result of the cement shrinkages and aggregate dilatations, which is defined as a nonlinear monotone increasing function as [49]:

$$\alpha^{th}(T) = \begin{cases} \alpha_0^{th} \frac{10}{10-\theta} & \text{if } T \leq 600 \ ^\circ\text{C}, \\ 0 & \text{if } T > 600 \ ^\circ\text{C}. \end{cases} \quad (4)$$

where α_0^{th} is the initial value at room temperature [8] and $\theta = T/100$ is the relative temperature level.

The main contribution of this work locates at the definition of the mesoscopic deformation to capture the macroscopic LITS in both load and unloaded directions of specimen under multiaxial compression stresses. The LITS, given by the sum of the two terms $\dot{\mathbf{e}}^v$ and $\dot{\mathbf{e}}^{thm}$ at the mesoscale [24], is determined experimentally by measuring total strains during first time heating on a concrete specimen under sustained loading and subtracting from that the free thermal strain, recorded on an unstressed specimen, and the initial elastic strain. Thelandersson [17] proposed a rheological macroscopic model for the LITS rate that in the uniaxial setting is given by two terms corresponding to a dashpot and a thermo-mechanical element, which are termed temperature dependent creep and thermo-mechanical strain, respectively. The two terms cannot be separated experimentally, this subdivision is mainly theoretical and has little practical implications for short duration heating [4]. However, the two components have different properties, e.g. the creep component takes place under both heating and cooling, and shows creep recovery, whereas the thermo-mechanical strain is only experienced during first heating and not during subsequent cooling or heating, and it is irrecoverable. Thelandersson [17] assumed that the creep strain is negligible in comparison with the thermo-mechanical strain for laboratory test conditions even though steady-state creep may be enhanced by high temperatures. If the temperature increase is not slow and the duration of the experimental test is limited to few hours the creep contribution can be neglected, as also showed in [18]. In the development of the proposed model, the long-term behavior under heating is not considered and is left for a further studies. This research focuses only on the modeling of the thermo-mechanical strains.

Based on the experimental observations [5,21,23,24] and macroscopic models [26,27,36], it is convenient to defined the thermo-mechanical strain on facet under compression stress to increase with the raising stress and temperature. The challenge is the simulation of the LITS in the unloaded directions. As reported in the mesoscopic simulations [39–41], the thermal cracks are randomly smeared in the specimen without any external applied load, while the thermal cracks

in the specimen under uniaxial compression load appear parallel to the load direction. Additionally, the preferential orientation of thermal cracks increases with the increase of the compression load level. Based on those observations, one can argue that the LITS in unloaded directions are partially attributed to the crack opening that parallel to the load directions. Hence the contribution of tensile stress to the mesoscopic thermo-mechanical strain on each Facet should be considered as well. The increment of normal component of thermo-mechanical strain is written as:

$$\dot{\epsilon}^{thm} = [\dot{\epsilon}_N^{thm} \quad \dot{\epsilon}_M^{thm} \quad \dot{\epsilon}_L^{thm}] \quad (5)$$

in which, $\dot{\epsilon}_N^{thm}$ denotes the normal component with the expression of:

$$\dot{\epsilon}_N^{thm} = \frac{\dot{t}_N^-}{\max(\sigma_{c0}^T, |t_N^{s-}|)} \beta^{th} \dot{T} + \frac{\dot{t}_N^+}{\sigma_t^T} \gamma^{th} \dot{T} \quad (6)$$

in which, the coefficient of $\beta^{th} = 0.01 \times (2A^{thm}\theta + B^{thm})$ is for compression and the coefficient of $\gamma^{th} = \theta^2 \beta^{th}$ is for tension, A^{thm} and B^{thm} are material parameters, σ_{c0}^T is the temperature-dependent mesoscopic yielding compressive stress, and σ_t^T is the temperature-dependent mesoscopic tensile strength. These two mesoscopic mechanical parameters are in detail described in Section 2.3.

For the case of facet under compression, the normal component ($\dot{\epsilon}_N^{thm}$) decreases with the temperature and the normal compressive stress that is calculated as $t_N^- = (t_N^s - |t_N^{s-}|)/2$. At the mesoscale level, the pure compressive stress can exceed the yielding compressive stress (σ_{c0}) due to the pore collapse and material compaction. Hence, based on previous studies, the ratio of t_N^- over $\max(\sigma_{c0}, |t_N^{s-}|)$ is defined to obtain the maximum of the unit in the plastic stage. For the case of facet under tension, the normal thm increases with the temperature and the tensile stress that is defined as $t_N^+ = (t_N^s + |t_N^{s-}|)/2$.

To simulate the macroscopic volumetric expansions in the unloaded directions, the shear components ($\dot{\epsilon}_M^{thm}$ and $\dot{\epsilon}_L^{thm}$) on facet under shear status is indispensable. These deviatoric strains does not impose volumetric strain directly, but can relax the mesoscopic shear stress lock caused by the incompatibility between the tension and compression normal thermal strains [50], which is illustrated in Fig. 1(c). Note that, for free thermal expansion, the normal thermal strains are compatible and no shear stress lock exists. Therefore, the shear components of $\dot{\epsilon}^{thm}$ are defined as:

$$\dot{\epsilon}_M^{thm} = \frac{\dot{t}_M^s}{\max(t_M^s, \sigma_s^T)} \beta^{th} \dot{T} \quad (7)$$

$$\dot{\epsilon}_L^{thm} = \frac{\dot{t}_L^s}{\max(t_L^s, \sigma_s^T)} \beta^{th} \dot{T} \quad (8)$$

in which, t_M^s and t_L^s are stress components in shear directions and the σ_s^T is the temperature-dependent mesoscopic shear strength which is detailedly defined in Section 2.3.

2.3. LDPM-HT constitutive laws

The mechanical strain is made up of temperature-dependent elastic strain and crack strain. The temperature-dependent elastic strain is computed by the thermal degradation of elastic modulus so as to capture the thermal degradation induced elastic strain increment, which is one component of LITS. The constitutive of LDPM-HT is briefly introduced in this section, and more details could be found in Shen et al. [9,29,42].

The LDPM elastic behavior is described by assuming that the tractions acting on the solid skeleton are proportional to the corresponding strains.

$$\mathbf{t}^s = [t_N^s \quad t_M^s \quad t_L^s]^T = [E_N e_N^s \quad E_T e_M^s \quad E_T e_L^s]^T \quad (9)$$

where, t_N^s , t_M^s , and t_L^s are the normal and shear components of the traction, $E_N = E_0^T$ and $E_T = \alpha^s E_0^T$. $E_0^T = \Lambda^{E_0}(T) E_0$ is the effective normal and shear elastic modulus at various temperatures with initial

effective normal elastic modulus (E_0) and the thermal degradation function $\Lambda^{E_0}(T)$. The shear-normal coupling parameter, α^s , deriving from the Poisson ratio typically takes the value of 0.25 for regular concrete [44].

The degradation function has the following expression:

$$\Lambda^A = 1 - \frac{\Theta e^{\eta_d^A}}{1 - \Theta(1 - e^{\eta_d^A})} \quad (10)$$

where the superscript Δ is the material parameter affected by high temperature, η_d^A governs the thermal degradation degree and $\Theta = (T - T_s^A)/(T_m^A - T_s^A)$ represents a normalized temperature level, in which T_s^A is the temperature at which concrete starts to degrade and T_m^A is the temperature at which material starts to melt. Since the individual effect of the different chemical/physical reactions at high temperature are not explicitly considered here, an overall calibration and validation are necessary for the three parameters of thermal degradation formula considering several experimental data. The superscript Δ in Eq. (10) represents a mesoscopic parameter, i.e. the elastic modulus E_0 , the tensile strength σ_t , the shear strength σ_s , the yielding compressive stress σ_{c0} , and the transitional stress σ_{N0} .

Fracturing and cohesive behavior for tension and tension/shear is simulated to occur for tensile deformation, i.e. $e_N^s > 0$. By defining the effective strain and the effective stress as $e^s = [e_N^{s2} + \alpha^s(e_M^{s2} + e_L^{s2})]^{1/2}$ and $t^s = [t_N^{s2} + (t_M^{s2} + t_L^{s2})/\alpha^s]^{1/2}$, one can write the relationship between stresses and strains through damage-type constitutive equations as $t_N^s = t^s e_N^s / e^s$, $t_M^s = \alpha^s t^s e_M^s / e^s$ and $t_L^s = \alpha^s t^s e_L^s / e^s$. The effective stress is assumed to be incrementally elastic $i^s = E_N e^s$ and limited by a strain-dependent boundary $0 \leq i^s \leq \sigma_{bt}(e^s, \omega)$. The mesoscopic tension stress boundary, $\sigma_{bt}(e^s)$, is defined as:

$$\sigma_{bt}(e^s, \omega) = \sigma_0(\omega) \exp \left[-H_0(\omega) \frac{\langle e_{\max}^s - e_0^s(\omega) \rangle}{\sigma_0(\omega)} \right] \quad (11)$$

where $\langle x \rangle = \max(x, 0)$, ω is the degree of interaction between shear and normal loading, which satisfies $\tan(\omega) = \sqrt{\alpha^s t_N^s / t_L^s}$, $e_T^s = (e_M^{s2} + e_L^{s2})^{1/2}$ and $t_T^s = (t_M^{s2} + t_L^{s2})^{1/2}$ are the total shear strain and stress, $e_{\max}^s(\tau)$ is the maximum effective strain in the loading history. The strength limit is defined as:

$$\sigma_0(\omega) = \sigma_t^T \frac{-\sin(\omega) + \sqrt{\sin^2(\omega) + 4\alpha^s \cos^2(\omega)/r_{st}^2}}{2\alpha^s \cos^2(\omega)/r_{st}^2} \quad (12)$$

where $r_{st} = \sigma_s^T / \sigma_t^T$ is the shear to tensile strength ratio at a given temperature. The effective softening modulus for post-peak is formulated as $H_0(\omega) = H_t(2\omega/\pi)^{n_t}$. Under pure tension, $H_0(\pi/2) = H_t = 2E_0^T/(l_t/l - 1)$ where H_t is the softening modulus, n_t is the softening exponent, $l_t = 2E_0 G_t/(\sigma_t^T)^2$ is the tensile characteristic length and G_t is the fracture energy. The tensile strength ($\sigma_t^T = \Lambda^{\sigma_t} \sigma_t$) and shear strength ($\sigma_s^T = \Lambda^{\sigma_s} \sigma_s$) deteriorate with the temperature increase assuming σ_t and σ_s , respectively, as their reference values at room temperature. The reference mesoscale tensile strength, σ_t , is generally first identified by fitting the macroscopic experimental data on fracture, such as three-point bending, wedge splitting, or Brazilian test. Whereas, the reference mesoscale shear strength, σ_s is identified by simulating the macroscopic compression behavior with low confinement [51,52].

For $e_N^s < 0$, the constitutive laws describe the pore collapse and material compaction in compression. The strain hardening plastic behavior due to high compressive hydrostatic deformation is described through a strain-dependent boundary $\sigma_{bc}(e_D^s, e_V^s)$ at each facet which limits the normal compressive stress component through the inequality $-\sigma_{bc}(e_D^s, e_V^s) \leq t_N^s \leq 0$, where $e_V^s = \Delta V^s/3V_0^s$ is the volumetric strain caused by stress, computed as the change between the current and the initial volume of each LDPM tetrahedron. Note that, for multi-physics coupling problems, the volumetric strain excludes the volume change caused by eigenstrains, e.g., the thermal expansion and drying shrinkage. The deviatoric strain $e_D^s = e_N^s - e_V^s$ varies from facet to facet.

For a constant deviatoric-to-volumetric strain ratio of $r_{DV} = e_D^s/e_V^s$, the compression stress boundary is defined as:

$$\sigma_{bc}(e_D^s, e_V^s) = \begin{cases} \sigma_{c0}^T, & -e_V^s \leq 0 \\ \sigma_{c0}^T + \langle -e_V^s - e_{c0} \rangle H_c(r_{DV}), & 0 \leq -e_V^s \leq e_{c1} \\ \sigma_{c1}(r_{DV}) \exp \left[(-e_V^s - e_{c1}) \frac{H_c(r_{DV})}{\sigma_{c1}(r_{DV})} \right], & \text{otherwise} \end{cases} \quad (13)$$

in which, $e_{c0} = \sigma_{c0}^T/E_0^T$ is the strain at which pore collapse starts, $e_{c1} = \kappa_{c0}e_{c0}$ is the strain at which rehardening starts, and $\sigma_{c1}(r_{DV}) = \sigma_{c0}^T + (e_{c1} - e_{c0})H_c(r_{DV})$. $\sigma_{c0}^T = \Lambda^{\sigma_{c0}}(T)\sigma_{c0}$ is the thermally degraded mesoscale yielding compressive stress with its initial value σ_{c0} . The slope of hardening modulus $H_c(r_{DV})$ is written as $H_{c0}/(1 + \kappa_{c2}\langle r_{DV} - \kappa_{c1} \rangle)$. H_{c0} , H_{c1} , κ_{c0} , κ_{c1} , κ_{c2} and κ_{c3} are model parameters. Typically, $H_{c0} = 0.4E_0^T$ and $\kappa_{c3} = 0.1$.

The frictional behavior due to compression-shear captures the increase in the shear strength under confined compression. The incremental shear stress in m and l directions are computed as $i_M^s = E_T(\dot{e}_M^s - \dot{e}_M^{sp})$, $i_L^s = E_T(\dot{e}_L^s - \dot{e}_L^{sp})$ where $\dot{e}_M^{sp} = \dot{\lambda}^s \partial \varphi_p / \partial t_M^s$, $\dot{e}_L^{sp} = \dot{\lambda}^s \partial \varphi_p / \partial t_L^s$, $\dot{\lambda}^s$ is the plastic multiplier and φ_p is the plastic potential, whose yielding surface is defined as:

$$\varphi_p = t_T^s - \left\{ \sigma_s^T - \mu_\infty t_N^s + (\mu_0 - \mu_\infty) \sigma_{N0}^T \left[1 - \exp \left(\frac{t_N^s}{\sigma_{N0}^T} \right) \right] \right\} \quad (14)$$

where μ_0 and $\mu_\infty = 0$ are the initial and final internal friction coefficients, $\sigma_{N0}^T = \Lambda^{\sigma_{N0}}(T)\sigma_{N0}$ is the normal stress with thermal damage which corresponds to the transition from μ_0 to μ_∞ .

3. Numerical example: uniaxial compression load

In this Section the proposed numerical model is applied to simulate the deformation evolution in concrete at high temperature under compressive uniaxial loading. Although in the literature there are same recent experimental research [53,54], the well-known test series performed by Anderberg and Thelandersson [20,21] is the most comprehensive so far, which includes the valuable thermal degradations tests, here used for the model calibration, the thermal deformations tests under constant loads and the mechanical responses tests under uniaxial restraint, here adopted for the model validation. For this reason, the old experimental tests in Anderberg and Thelandersson [20,21] are numerically simulated in the present study.

3.1. Experimental and numerical setup

The modified LDPM-HT is applied to the mesoscale analyses of the macroscopic phenomenon of thermal deformation, which is the sum of the free thermal strain, the elastic strain increments due to thermal degradation, and the thermo-mechanical strain. Experimental results obtained by Anderberg and Thelandersson [20,21] show that there is no significant influence of the rate of temperature increase for rates of 1 and 5 °C/min. This indicates that the temperature loading in these experiments is slow enough to neglect the influence of the thermal capacity of the materials. Therefore, the thermal analysis is simplified by assuming a uniform temperature increase throughout the specimen, disregarding the thermal conductivity and capacity. On the other hand, the temperature rates of 1 up to 5 °C/min are fast enough to neglect the time-dependent effects [18].

A concrete cylinder with 150 mm height and 75 mm diameter is chosen as the same dimension of specimen in experiment [20,21]. The coarse aggregate volume fraction is computed based on the mix composition as listed in Table 1. A maximum aggregate diameter of 12 mm, as in the concrete used in the experimental campaign, and a minimum aggregate diameter of 4 mm are adopted for the generation of the LDPM mesh. The size of the minimum aggregate diameter is chosen by the authors. The minimum aggregate size governs the resolution of the model

Table 1

Concrete mix-designs and model parameters used in the simulations.

Parameters	Unit	Definition	Sect. 3	Sect. 4
Mix-designs				
c	[kg/m ³]	Cement content	390	390
w_{mix}/c	[-]	Water/cement ratio	0.6	0.6
a/c	[-]	Agg./cement ratio	3.0	3.0
d_a	[mm]	Agg. maximum diameter	12	12
LDPM at room temperature				
E_0	[MPa]	Normal Modulus	42500	45000
σ_t	[MPa]	Tensile strength	4	5
l_t	[mm]	Tensile charact. length	120	120
σ_s	[MPa]	Shear strength	12	17
σ_{c0}	[MPa]	Compressive yielding stress	140	150
μ_0	[-]	Initial friction	0.4	0.2
σ_{N0}	[MPa]	Transitional stress	600	600
κ_{c0}	[-]	Strain limit ratio	5	5
κ_{c1}	[-]	Vol. dev. damage threshold ratio	1	1
κ_{c2}	[-]	Vol. dev. damage magnitude	2	2
d_0	[mm]	Agg. minimum diameter in LDPM	4	4
LDPM at high temperature				
α_0	[°C ⁻¹]	Initial thermal expansion coeff.	7	8.5
A^{thm}	[-]	Coeff. for e^{thm}	0.0035	0.0004
B^{thm}	[-]	Coeff. for e^{thm}	0.001	0.001

and, consequently, the number and direction of the possible crack paths in the meso-structure. Clearly, with a small minimum aggregate size, it is possible to reproduce fine features of crack initiation and propagation in the meso-structure, but at the same time, the computational cost tends to be very high [42,44]. Since no precautionary smoothing or friction reduction material is reported in the description of the tests, the high friction condition between the cylinder ends and the platens are modeled through a friction coefficient, μ , which is function of the slippage, s , as $\mu(s) = \mu_d + (\mu_s - \mu_d)s_0/(s + s_0)$ with $\mu_s = 0.13$, $\mu_d = 0.015$ and $s_0 = 1.3$ mm. The geometry, loading setup, and mesh discretization are illustrated in Fig. 2.

Three types of loading conditions are considered: (1) the concrete specimen subjected to monotonic uniaxial compression at various temperatures (in this step the parameters that govern the material mechanical properties and their thermal degradation evolutions are calibrated and validated); (2) the specimen heated while subject to various levels of constant uniaxial compressive stress (here the parameters of free thermal strain and thermo-mechanical strain are calibrated); (3) the specimen subjected to uniform heating under uniaxial restraint (no fitting is performed in this phase and the proposed model can be validated). The results of all three loading scenarios are compared to the experimental results obtained by Anderberg and Thelandersson [21] as described in the following.

3.2. Uniaxial compression at high temperature

Numerical analyses of uniaxial compression tests at various temperatures are performed. The top platen applies the compressive displacement load to the cylinder specimen and the bottom is fixed that supports the specimen. The mesoscopic parameter of elastic modulus E_0 , tension strength σ_t and shear strength σ_s are determined by fitting the stress-strain curves at 20 °C. The parameters of thermal degradation are determined by fitting the stress-strain curves at 770 °C. The other parameters are defined based on the Ref. [9,42,44]. In Fig. 3, the stress-strain curves at other temperatures (400 °C, 500 °C, 650 °C) predicted by LDPM-HT are compared to the experimental data. These good agreements demonstrate the ability of LDPM-HT for capturing mechanical behaviors at various temperatures. Three meshes with different random aggregate distributions are simulated for each target temperature and their results are the dashed lines in Fig. 3. However, the average stress-strain curve (solid line) is adopted to fit

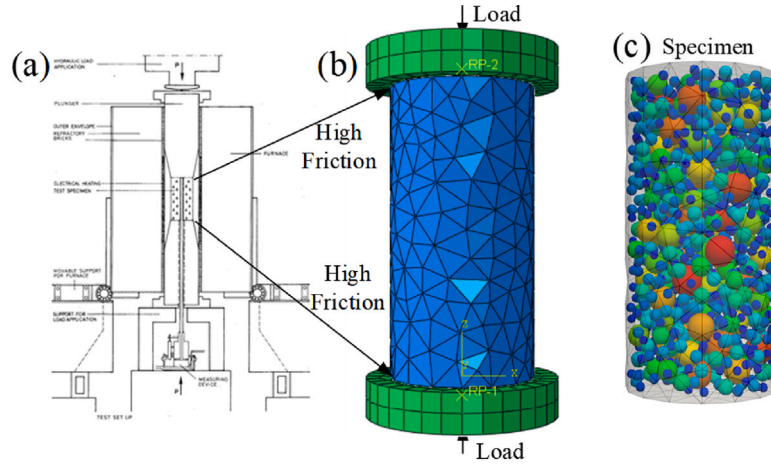


Fig. 2. Setup of uniaxial compressive load test. (a) Experiment; (b) simulation; (c) aggregate distribution.

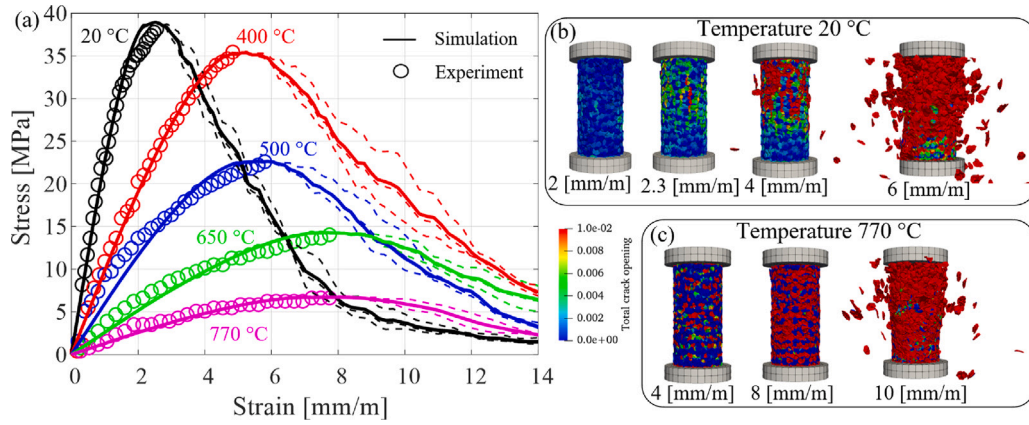


Fig. 3. Compression tests at various temperatures. (a) Stress vs. strain; (b) fracture patterns at 20 °C; (c) fracture patterns at 770 °C.

Table 2

Parameters for thermal degradation.

Para.	Definition	Start temp. T_s [°C]	Melt temp. T_m [°C]	Shape n_d [-]	Source
LDPM					
σ_t^T	Tensile strength	390	1000	1.1	Identified
σ_s^T	Shear strength	390	1000	1.1	Identified
E_0^T	Normal Modulus	100	800	0.8	Identified
σ_{c0}^T	Comp. yielding stress	300	1000	0.6	[9]
σ_{N0}^T	Transitional stress	300	1000	0.6	[9]

the experimental data (dot). All the model parameters are presented in Table 1 and 2 and are used in the following simulations.

The fracture patterns of specimens at 20 °C and 770 °C are displaced in Fig. 3(b) and (c), respectively. In the case of 20 °C, the cracks are mainly perpendicular to the loading direction at an early stage within the pre-peak regime (0 mm/m–2.3 mm/m), and their opening and number increase remarkably. Around the compression strain of 2.3 mm/m, a macro-crack occurs and the stress reaches the peak. A similar direction of crack propagation was observed in Grassl and Pearce [39] for the case of mini-scale simulation. At a post-peak stage, the concrete fragments gradually fall off from the specimen with the increase of compression load. In the end, the specimen collapses. In the case of 770 °C, the cracks distribution is more uniform than that of the case at 20 °C. This phenomenon means the preference of crack orientation becomes marginal due to the high temperature degradation, and thus results an increase of the material ductility at high temperature.

3.3. Thermal deformation under uniaxial compression

In the second group of tests the loading conditions are applied in two steps. First a uniaxial compression load of four different levels ($\text{Load}/f_c = 0, 0.225, 0.45, 0.675$) is imposed on the specimen whose compression strength, f_c , is 38 MPa. Then, keeping those stresses constant, the temperature is increased from 20 °C to 800 °C, while the deformations in the axial direction are measured.

The mechanical parameters in Tables 1 and 2 are used in these cases. The thermal expansion coefficient is determined from the best-fitting of the experimental result for the free-thermal expansion test, i.e. $\text{Load}/f_c = 0$. The coefficients of the thermo-mechanical strain (in Eq. (6)) are determined by fitting the experimental deformation in the loading direction under the stress level of $\text{Load}/f_c = 0.225$. The numerical simulations of the other two tests with $\text{Load}/f_c = 0.45$ and 0.675 are carried out with the calibrated parameters and no additional fits are performed. All the strain-temperature curves obtained for this the second group of tests using the LDPM-HT are compared to the experimental results in Fig. 4, demonstrating the effectiveness of the proposed model in reproduce the experimental observations.

The crack distributions for the four different loading cases are displaced in Fig. 4(b) and (c) as well. At the same temperature of 600 °C, the number and opening of crack both increase with the compression stress levels; see in Fig. 4(b). In Fig. 4(c), the number and opening of cracks increase with the temperature due to the combined effect of the thermal degradation, while the stress level of $\text{Stress}/f_c = 0.675$ is kept constant in Fig. 4(c). Before the specimen losses the bearing capability (490 °C), the distribution of cracks is more uniform than that in the specimen under uniaxial compression test in Fig. 3(b).

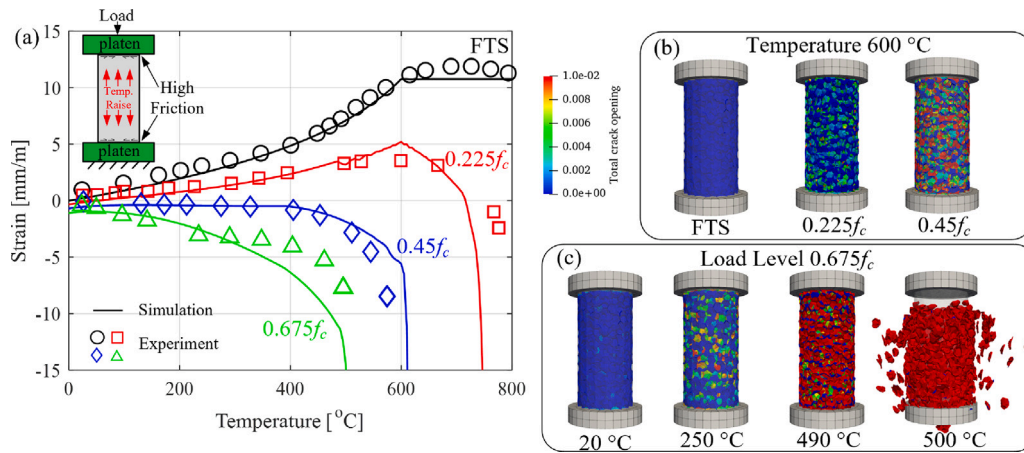


Fig. 4. Thermal deformation with various stress levels. (a) Compression strain vs. temperature; (b) Fracture patterns at 600 °C; (c) Fracture patterns at with Load/ $f_c = 0.675$.

3.4. Mechanical behavior under uniaxial restraint

In the third group of experimental tests that are numerically simulated, the specimen is restrained in the axial direction while the temperature is increased from the ambient temperature of 20 to 1000 °C. The same material properties in Tables 1 and 2 as in the previous example are adopted, i.e. no parameter calibration is performed in this section. The normalized average stress obtained from the analysis is plotted against temperature in Fig. 5(a) and compared with the experimental results of Anderberg and Thelandersson [21]. The fracture distributions obtained in the numerical analysis are shown in Fig. 5(b) as well.

Initially, the compressive stresses raise steeply below 100 °C and then slowly reaches the maximum stress level ($0.42f_c$) at approximately 400 °C. This remarkable decrease of stress increasing rate is caused by the thermal degradation of the elastic properties beyond 100 °C. In this temperature range (up to 400 °C) the LDPM-HT predicts a higher stress level than the one observed in the experimental investigation. This stress overestimation is mainly caused by the assumption of applying a uniform temperature increase in the sample neglecting the transient heat transfer and mass transport processes. The drying shrinkage caused by the moisture loss can partially counteract the thermal expansion and the no uniform temperature distribution results in a relative small total thermal expansion. To take into account those phenomena, a full thermo-hygro-mechanical coupled model is needed and this is left for future research work.

Then the compressive stress reduces with further temperature increase, since the mesoscopic mechanical parameters ($\sigma_t, \sigma_s, \sigma_{N0}$) start to degrade at the temperature range of 300 °C and 400 °C, respectively. At 500 °C and 620 °C, the stress drops significantly due to the fragments spalled-off from the specimen (see in Fig. 5). For the case of 500 °C, the stress increases again due to the further expansion of the specimen. The specimen almost loses the bearing capability at 800 °C.

It should be noted that the model parameters adopted in this case are not fitted to match the experimental results. Nevertheless, the mesoscale modeling approach in this work captures satisfactorily the mechanical behavior observed in the experiments.

4. Numerical example: multiaxial compressive loads test

In this Section, a numerical example is solve to verify the capability of the proposed constitutive model to simulate the behaviors of concrete under true multiaxial loading conditions. In this regard, the representative experimental tests carried out by Petkovski and Crouch [23] investigating the thermal deformations under different multiaxial boundary conditions are considered.

4.1. Experimental and numerical setup

The considered experimental investigation was performed on the mac^{2T} apparatus at the University of Sheffield (Fig. 6(a)), a facility able to test 100 mm cubic concrete specimens under multiaxial compression loads (up to 400 MPa) and, simultaneously, with temperatures up to 300 °C. The uniaxial, biaxial, and hydrostatic compressive stress can be applied to concrete specimen sides through six steel platens, which are also able to transfer heat to the specimen by conduction. In the numerical simulations of this section first the thermal deformations of the specimen subjected to a compressive stress of 26.9 MPa and then heated up to 250 °C with a rate of 0.2 °C/min are simulated. As explained in the previous section, the thermal analyses are performed with a uniform temperature increase throughout the specimen. A concrete cube with 101 mm side length is chosen as the same dimension of specimen used in experimental study [23], see Fig. 6. The distribution of aggregates was obtained with maximum diameter of 12 mm and minimum diameter of 4 mm. The high friction condition between the specimen surfaces and the platens is considered (Section 3). The geometry, loading setup, and mesoscale mesh discretization adopted in the numerical simulations are shown in Fig. 6(b) and (c). The mechanical parameters (Table 1) at ambient temperature are chosen to obtain a compressive strength of $f_c = 59$ MPa as reported in [23]. The parameters for thermal degradations in Table 2, that has been calibrated in the previous Section, are also used here because there is no available data on mechanical response at high temperature in [23].

4.2. Thermal deformation under multiaxial compression

The proposed model is here applied to simulate the multiaxial transient tests performed within the experimental campaign presented in [23]. Fig. 7 shows the experimental and numerical thermal deformation as a function of the heating time. The temperature linearly increases up to the maximum of 250 °C at the time of 1250 min. Four cases with the same heating loads are considered. Because the duration of the experimental tests is less than 24 h the initial assumption of neglecting the creep strain is fully justified.

The linear expansion coefficient accounting for the free thermal strain and the coefficients accounting for the mesoscopic thermo-mechanical strain are calibrated by fitting the transient tests performed under the “free” and the uniaxial compression load condition, respectively. For the first case, the mesoscopic thermal expansion coefficient is determined by fitting the measured macroscopic free thermal expansion of specimen under a small hydrostatic compressive stress of 0.9 MPa, see in Fig. 7(a). For the second, the parameters characterizing the mesoscopic thermo-mechanical strain in Eqs. (6) and (7) are determined by fitting the thermal deformations of specimen under the

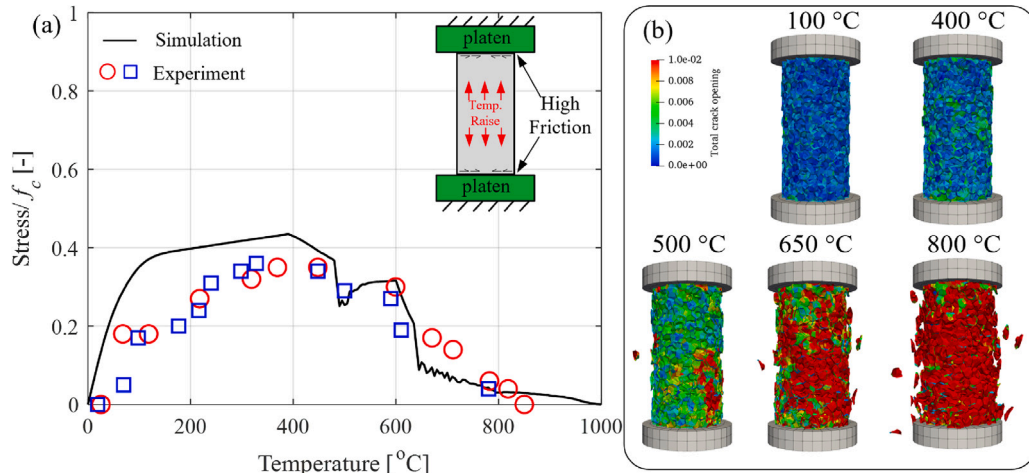


Fig. 5. Mechanical responses under uniaxial restraint. The fracture patterns at different stages (a–f) are all marked on the simulation results.

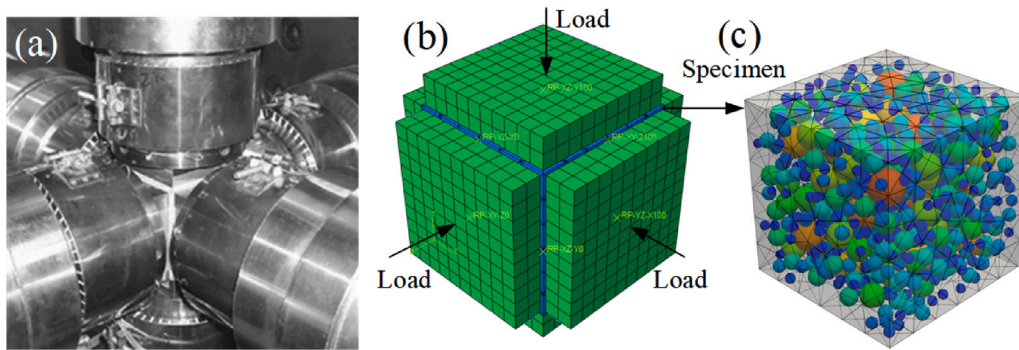


Fig. 6. Setup of multi-axial test. (a) mac^{2T} apparatus; (b) numerical test; (c) aggregate distribution.

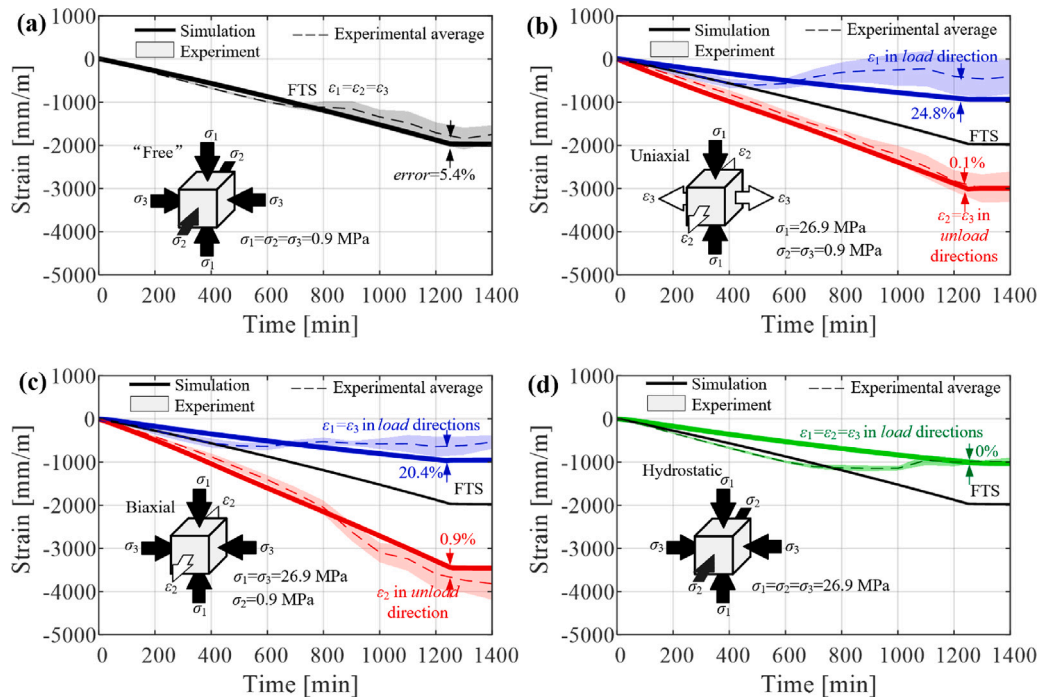


Fig. 7. Thermal deformation (negative strain represents expansion) under multi-axial compression loading conditions: (a) unloaded; (b) uniaxial; (c) biaxial; (d) triaxial.

uniaxial compressive stress of 26.9 MPa, see in Fig. 7(b). The dash and solid lines are the numerical predictions of thermal deformation without and with the consideration of LITS, respectively. The shadow areas are the experimental measurements in both the loaded and unloaded directions. One can clearly observe that the “expansion” in the loading direction has a significant decrement due to the presence of the compression load, while the expansions in the unloaded directions show significant increments. The agreement between the experiments and simulations demonstrates that the proposed model is able to capture the thermal deformations in both loaded and unloaded directions.

The calibrated model is next validated by modeling transient tests performed under biaxial and triaxial compression loading. For the validation phase, the LDPM-HT is used to simulated the thermal deformations of specimens under equal biaxial and hydrostatic compressive stresses without any further adjustment of the material parameters. As shown in Figs. 7 (c) and (d), the agreements between the experiment and numerical thermal deformations in both load directions (26.9 MPa) and load-free directions (0.9 MPa) verifies the accuracy of the proposed mesoscopic constitutive model in the simulation of the thermal strain at high temperature.

Although the proposed model can satisfactorily reproduce all the experimental results, one cannot deny that it does not perfectly predict the deformations in all directions. To quantify them, a relative error is defined as the derivation of the absolute difference between simulation and experiment over the experimental free thermal strain ($|e_{sim} - e_{exp}|/|e_{exp}^{fr}|$) at the target temperature (250 °C). This error is calculated for each test simulated and reported in Fig. 7. One can see that the large errors are observed for the deformations in the loaded directions for uniaxial and biaxial loading conditions (i.e. Fig. 7(b) and (c)) after 600 min of heating (120 °C). This lack of accuracy in the model prediction can be explained by the simplification used to model the drying shrinkage caused by the evaporation and migration of moisture which is not uniform in the sample cross section.

5. Conclusions

The mesoscopic thermo-mechanical deformation is implemented within the framework of Lattice Discrete Particle Model of concrete at high temperature (LDPM-HT) so as to capture the Load Induce Thermal Strain (LITS). The LITS is decoupled into the creep strain rate and the thermo-mechanical strain at the mesoscale. As a first extension of the LDPM-HT model the long term effect of the creep is neglected and only the thermo-mechanical strain is taken into account for the first heating. In the proposed approach the thermo-mechanical strain is decomposed into the normal compression, normal tension and shear components at the meso-scale. The mesoscopic normal thermo-mechanical strain under compression controls the macroscopic LITS in the compression load direction, while the normal thermo-mechanical strain under tension and the thermo-mechanical shear strains governs the LITS in the unloaded directions.

The calibrations and validations of the updated LDPM-HT are performed by simulating two experimental investigation from the literature, namely a series of tests with uniaxial load and temperatures up to 800 °C and a second a series of tests with multiaxial compressive loads and temperatures up to 250 °C. The improved LDPM-HT not only captures the experimentally observed dependency of LITS on temperature and stress confinement in both load and unloaded directions, but also the mechanical responses of specimen under various stress levels and temperature conditions. These excellent agreements between the numerical and the experimental results demonstrates the reliability and accuracy of the improved LDPM-HT.

The present work is a part of the development of a discrete thermo-hygro-mechanical coupled model of concrete at high temperature [9, 29, 42]. Although the proposed model provides overall good results, some small limitations has been observed that will require further work to study the effect of transient heat transfer and water mass transport on the LITS, e.g., specimen size, drying shrinkage and time-dependent creep.

CRediT authorship contribution statement

Lei Shen: Conceptualization, Methodology, Software, Investigation, Validation, Writing – original draft, Writing – review & editing, Funding acquisition. **Huayi Zhang:** Methodology, Software, Investigation, Writing – review & editing. **Giovanni Di Luzio:** Methodology, Software, Investigation, Writing – review & editing. **Hao Yin:** Methodology, Software, Investigation, Writing – review & editing. **Lifu Yang:** Methodology, Software, Investigation, Writing – review & editing. **Gianluca Cusatis:** Methodology, Software, Investigation, Writing – review & editing.

Declaration of competing interest

The authors declare that they have no known competing financial interests or personal relationships that could have appeared to influence the work reported in this paper.

Data availability

Data will be made available on request.

Acknowledgments

The work of the first and second authors was supported by the National Natural Science Foundation of China (51908195), and Fundamental Research Funds for the Central Universities, China (B220201030, B220204001).

References

- [1] Di Luzio G, Biolzi L. Assessing the residual fracture properties of thermally damaged high strength concrete. *Mech Mater* 2013;64:27–43.
- [2] Biolzi L, Di Luzio G, Labuz JF. Mechanical properties of photocatalytic white concrete subjected to high temperatures. *Cem Concr Compos* 2013;39:73–81.
- [3] Hansen TC, Eriksson L. Temperature change effect on behavior of cement paste mortar, and concrete under load. *ACI J* 1966;63:489–504.
- [4] Schneider U. Concrete at high temperatures - A general review. *Fire Saf J* 1988;13:55–68.
- [5] Khoury G, Sullivan P, Grainger B. Transient thermal strain of concrete: Literature review, conditions within specimen and behaviour of individual constituents. *Mag Concr Res* 1985;37:131–44.
- [6] Lea F. The resistance to fire of concrete and reinforced concrete. *J Soc Chem Ind* 1922;41(18):395R–6R.
- [7] Law A, Gillie M. Load induced thermal strains: implications for structural behaviour. In: Kang H, Kodur VKR, Tan TH, editors. *Proceedings of the fifth international conference structures in fire*. Singapore: Nanyang Technological University, Organising Committee; 2008.
- [8] Bažant ZP, Kaplan MF. Concrete at high temperatures: material properties and mathematical models. Longman; 1996.
- [9] Shen L, Li W, Zhou X, Feng J, Di Luzio G, Ren Q, et al. Multiphysics lattice discrete particle model for the simulation of concrete thermal spalling. *Cem Concr Compos* 2020;106:103457.
- [10] Pickett GT. The effect of change in moisture content on the creep of concrete under a sustained load. *J Am Concr Inst* 1942;38:333–55.
- [11] Di Luzio G, Cusatis G. Solidification-Microprestress-Microplane (SMM) theory for concrete at early age: Theory, validation and application. *Int J Solids Struct* 2013;50(6):957–75.
- [12] Di Luzio G, Cedolin L, Beltrami C. Tridimensional long-term finite element analysis of reinforced concrete structures with rate-type creep approach. *Appl Sci* 2020;10(14).
- [13] Illston JM, Sanders PD. The effect of temperature change upon the creep of mortar under torsional loading. *Mag Concr Res* 1973;25(84):136–44.
- [14] Bažant ZP, Cusatis G, Cedolin L. Temperature effect on concrete creep modeled by microprestress-solidification theory. *J Eng Mech* 2004;130(6):691–9.
- [15] Bažant ZP, Hauggaard AB, Baweja S, Ulm FJ. Microprestress-solidification theory for concrete creep. I: Aging and drying effects. *J Eng Mech* 1997;123:1188–94.
- [16] Masoero E, Di Luzio G. Nanoparticle simulations of logarithmic creep and microprestress relaxation in concrete and other disordered solids. *Cem Concr Res* 2020;137:106181.
- [17] Thelandersson S. Modeling of combined thermal and mechanical action in concrete. *J Eng Mech* 1987;113:893–906.

- [18] Nielsen CV, Pearce CJ, Bicanic N. Improved phenomenological modeling of transient thermal strains for concrete at high temperatures. *Comput Concr* 2004;1(2):189–209.
- [19] Sabeur H, Meftah F. Dehydration creep of concrete at high temperatures. *Mater Struct* 2008;41:17–30.
- [20] Anderberg Y, Thelandersson S. Stress and deformation characteristics of concrete at high temperatures. 1. General discussion and critical review of literature. In: *Bulletin of division of structural mechanics and concrete construction*, vol. Bulletin 34, 1973.
- [21] Anderberg Y, Thelandersson S. Stress and deformation characteristics of concrete at high temperatures. 2. Experimental investigation and material behaviour model. In: *Bulletin of division of structural mechanics and concrete construction*, vol. Bulletin 54, 1976.
- [22] Schneider U. Behaviour of concrete under thermal steady state and non-steady state conditions. *Fire Mater* 1976;1:103–15.
- [23] Petkovski M, Crouch R. Strains under transient hygro-thermal states in concrete loaded in multiaxial compression and heated to 250 °C. *Cem Concr Res* 2008;38(4):586–96.
- [24] Mindeguia J-C, Hager I, Pimentia P, Carré H, La Borderie C. Parametrical study of transient thermal strain of ordinary and high performance concrete. *Cem Concr Res* 2013;48:40–52.
- [25] Bažant ZP, Chern JC. Stress-induced thermal and shrinkage strains in concrete. *J Eng Mech* 1987;113:493–511.
- [26] Torelli G, Mandal P, Gillie M, Tran V-X. Concrete strains under transient thermal conditions: A state-of-the-art review. *Eng Struct* 2016;127:172–88.
- [27] Gernay T, Millard A, Franssen J-M. A multiaxial constitutive model for concrete in the fire situation: Theoretical formulation. *Int J Solids Struct* 2013;50(22):3659–73.
- [28] Buttignol TET, Bittencourt TN. Simplified design procedures for the structural analysis of reinforced concrete columns in fire. *Eng Struct* 2021;246:113076.
- [29] Shen L, Lo Monte F, Di Luzio G, Cusatis G, Ren Q. On the moisture migration of concrete subject to high temperature with different heating rates. *Cem Concr Res* 2021;146:106492.
- [30] Gawin D, Pesavento F, Schrefler B. Modelling of deformations of high strength concrete at elevated temperatures. *Mater Struct* 2004;37:218.
- [31] Kordina K, Ehm C, Schneider U. Effects of biaxial loading on the high temperature behaviour of concrete. *Fire Saf Sci* 1986;1:281–90.
- [32] Ehm C, Schneider U. The high temperature behaviour of concrete under biaxial conditions. *Cem Concr Res* 1985;15(1):27–34.
- [33] de Borst R, Peeters PP. Analysis of concrete structures under thermal loading. *Comput Methods Appl Mech Engrg* 1989;77(3):293–310.
- [34] Nechnech W, Meftah F, Reynouard J. An elasto-plastic damage model for plain concrete subjected to high temperatures. *Eng Struct* 2002;24(5):597–611.
- [35] Pearce CJ BN. Gradient enhanced thermo-mechanical damage model for concrete at high temperatures including transient thermal creep. *Int J Numer Anal Methods Geomech* 2004;28:715–35.
- [36] Torelli G, Gillie M, Mandal P, Tran V-X. A multiaxial load-induced thermal strain constitutive model for concrete. *Int J Solids Struct* 2017;108:115–25.
- [37] Torelli G, Mandal P, Gillie M, Tran V-X. A confinement-dependent load-induced thermal strain constitutive model for concrete subjected to temperatures up to 500 °C. *Int J Mech Sci* 2018;144:887–96.
- [38] Torelli G, Gillie M, Mandal P, Draup J, Tran V-X. A moisture-dependent thermomechanical constitutive model for concrete subjected to transient high temperatures. *Eng Struct* 2020;210:110170.
- [39] Grassl P, Pearce C. Mesoscale approach to modeling concrete subjected to thermomechanical loading. *J Eng Mech* 2010;136:322–8.
- [40] Pham D, Trong Dung N, Vu N, Chinkulkijniwat A. Mesoscale approach to numerical modelling of thermo-mechanical behaviour of concrete at high temperature. *Eur J Environ Civ Eng* 2019;25:1–20.
- [41] Buttignol TE, Bitencourt Jr LA. A transient creep investigation applied to the mesoscopic analysis of plain concrete under uniaxial compression at high temperature. *Fire Saf J* 2021;126:103484.
- [42] Shen L, Di Luzio G, Zhu D, Yao X, Cusatis G, Cao M, et al. Mechanical responses of steel fiber-reinforced concrete after exposure to high temperature: Experiments and mesoscale discrete modeling. *J Eng Mech* 2021;147(11):04021084.
- [43] Cusatis G, Pelessone D, Mencarelli A. Lattice discrete particle model (LDPM) for failure behavior of concrete. I: Theory. *Cem Concr Compos* 2011;33(9):881–90.
- [44] Cusatis G, Mencarelli A, Pelessone D, Baylot J. Lattice discrete particle model (LDPM) for failure behavior of concrete. II: Calibration and validation. *Cem Concr Compos* 2011;33(9):891–905.
- [45] Alnaggar M, Di Luzio G, Cusatis G. Modeling time-dependent behavior of concrete affected by alkali silica reaction in variable environmental conditions. *Materials* 2017;10(5):471.
- [46] Yang L, Pathirage M, Su H, Alnaggar M, Di Luzio G, Cusatis G. Computational modeling of expansion and deterioration due to alkali-silica reaction: Effects of size angle, size distribution, and content of reactive aggregate. *Int J Solids Struct* 2022;234–235:111220.
- [47] Yang L, Pathirage M, Su H, Alnaggar M, Di Luzio G, Cusatis G. Computational modeling of temperature and relative humidity effects on concrete expansion due to alkali-silica reaction. *Cem Concr Compos* 2021;124:104237.
- [48] Khoury G. Strain components of nuclear-reactor-type concretes during first heat cycle. *Nucl Eng Des* 1995;156:313–21.
- [49] Pearce C, Nielsen C, Bicanic N. Theoretical model of high temperature effects on uniaxial concrete member under elastic restraint. *Mag Concr Res* 2002;54:239–49.
- [50] Bolander JE, Eliáš J, Cusatis G, Nagai K. Discrete mechanical models of concrete fracture. *Eng Fract Mech* 2021;257:108030.
- [51] Angiolilli M, Pathirage M, Gregori A, Cusatis G. Lattice discrete particle model for the simulation of irregular stone masonry. *J Struct Eng* 2021;147(9):04021123.
- [52] Cibelli A, Pathirage M, Cusatis G, Ferrara L, Di Luzio G. A discrete numerical model for the effects of crack healing on the behaviour of ordinary plain concrete: Implementation, calibration, and validation. *Eng Fract Mech* 2022;263:108266.
- [53] Alogla S, Kodur V. Temperature-induced transient creep strain in fiber-reinforced concrete. *Cem Concr Compos* 2020;113:103719.
- [54] Fan K, Li J, He Z, Liu Q, Yao Y. Transient creep strain of fly ash concrete at elevated temperatures. *Mag Concr Res* 2022;1–12.